Control of a Novel 2-DoF MEMS Nanopositioner With Electrothermal Actuation and Sensing.

Micky Rakotondrabe, Anthony Fowler, S.O. Moheimani

Control of a Novel 2-DoF MEMS Nanopositioner with Electrothermal Actuation and Sensing

Micky RAKOTONDRABE [1], *Member, IEEE*, Anthony G. FOWLER [2], *Student Member, IEEE*, and S. O. Reza MOHEIMANI [2], *Fellow, IEEE*

***Abstract*—This paper presents the full characterization, modeling, and control of a 2-degree of freedom microelectromechanical systems (MEMS) nanopositioner with fully integrated electrothermal actuators and sensors. Made from nickel Z-shaped beams, the actuators are able to move the device's stage in positive and negative directions (contrary to classical V-shaped electrothermal actuators) and along two axes (x and y). The integrated electrothermal sensors are based on polysilicon resistors, which are heated via Joule heating due to an applied electrical bias voltage. The stage displacement is effectively measured by variations in their resistance, which is dependent on the position of the stage. The characterization tests carried out show that the MEMS nanopositioner can achieve a range of displacement in excess of $\pm 5\mu m$ for each of the x and y axes, with a response time better than $300ms$. A control scheme based on the combination of feedforward and IMC-feedback is constructed in order to enhance the general performance of the MEMS device, and in particular to reject the cross-coupling between the two axes and to enhance the accuracy and the response time. The experimental results demonstrate the efficiency of the proposed scheme and demonstrate the suitability of the designed device for nanopositioning applications.**

***Index Terms*—2-DoF MEMS nanopositioner, electrothermal actuators, electrothermal sensors, feedforward feedback control, IMC control scheme, nanopositioning.**

I. INTRODUCTION

ONE of the fundamental requirements of many microscale and nanoscale applications is the ability to provide high-precision motion with nanometer resolution. An important example is the atomic force microscope (AFM) [1], a form of scanning probe microscopy [2]. A nanopositioning system is one of the main elements of the AFM, where it is used to move the sample in a raster pattern while measurements of the sample's topography are made using a cantilever with a sharp probe. The ability of nanopositioners to provide precise mechanical displacements has also seen them used in novel applications such as in high-density probe-based data storage systems [3], [4].

Nanopositioners based on microelectromechanical systems (MEMS) fabrication processes possess a number of potential advantages compared with macro-scale nanopositioners including lower fabrication costs, a smaller overall footprint, ease of bulk fabrication and increased bandwidth [5], [6]. A novel MEMS nanopositioner for AFM applications was demonstrated in [7], with the device acting as the scanning stage for a commercial AFM. A series of gold features was designed as part of the device's stage to represent a scan sample, and an image of the features was successfully obtained via an open-loop scan performed in tapping mode.

Two commonly-used mechanisms for achieving mechanical displacements in MEMS-based devices are electrothermal and electrostatic actuators [8]. While both are relatively straightforward to implement without the need for complex fabrication processes, electrothermal actuators have the advantage of being able to provide high actuation forces while maintaining a relatively small footprint [9], [10]. This has led to their increasing development and utilization in MEMS-based nanopositioning applications over recent years.

One of the most commonly-used forms of in-plane electrothermal actuator is the V-shaped, or "chevron" type actuator, which has been demonstrated in a wide range of MEMS applications [5], [11]–[13]. This type of actuator typically features a series of bent conductive beams through which a current is passed. Joule heating results in the thermal expansion of these beams, which creates a mechanical displacement in the direction in which the beams are bent. A disadvantage of this mechanism is that the angled arrangement of the beams results in a high mechanical stiffness in the reverse direction, meaning that it is impractical to connect two actuators back-to-back to achieve bidirectional motion.

The use of a new type of MEMS electrothermal actuator with Z-shaped beams has recently been demonstrated [9], [14]–[16]. While the basic principle of operation is similar to the conventional actuator with V-shaped beams, the configuration of the Z-shaped beams means that the mechanism's mechanical stiffness in the reverse direction is similar to that in the direction of actuation. This means that two actuators can be effectively coupled back-to-back to create a structure that possesses bidirectional motion.

This paper presents a novel MEMS nanopositioner that uses these novel Z-shaped electrothermal actuators to move a central stage. Four actuators are used to facilitate bidirectional positioning along two axes, resulting in a 2-degree of freedom (DoF) system. Integrated electrothermal displacement sensors are used to measure the displacement of the stage along each axis, allowing for closed-loop control of the system. Electrothermal sensing has been demonstrated in a growing

[1]: FEMTO-ST Institute, UMR CNRS 6174 - UFC / ENSMM / UTBM, Automatic Control and Micro-Mechatronic Systems depart., AS2M, 25000 Besançon - France (e-mail: mrakoton@femto-st.fr). This research was performed when the first author was on study leave at the University of Newcastle.

[2]: Laboratory for Dynamics and Control of Nanosystems, School of Electrical Engineering and Computer Science, University of Newcastle, Callaghan, NSW 2308, Australia (email: Anthony.Fowler@uon.edu.au, Reza.Moheimani@newcastle.edu.au)

Paper type: regular paper.

number of MEMS applications [11], [17], [18], and represents a compact and easily-implemented solution for integrated position measurement that is able to provide sub-nanometer resolution [19].

The paper is organized as follows. In section II, the principle of operation and the design and characterization of the 2-DoF MEMS nanopositioner are presented. The characterization shows that the nanopositioner is typified by a static nonlinearity between the applied voltage and the output displacement, and that cross-couplings exist between the two axes. In order to obtain a general linear model, we therefore propose first a feedforward controller in Section III. Then, we present in section IV the closed-loop control of the linearized system in order to enhance its performance in terms of accuracy and response time, and to reject the cross-couplings between the two axes of the device. For that, we demonstrate that internal model control (IMC) can efficiently be employed.

II. The MEMS nanopositioner

A. Principle of operation

The schematic diagram in Fig. 1-a displays the principle of operation of the MEMS nanopositioner in one DoF. The device is comprised of two sets of nickel Z-shaped beams that serve as the actuators used to position the stage, and two polysilicon sensors placed underneath this movable stage. Beneath each set of actuator beams is a polysilicon electrothermal heater (not pictured in the figure) which provides the thermal energy required for actuation.

One actuator, consisting of a set of Z-shaped beams, is used to create movement in one direction (i.e. the positive direction or negative direction). For instance, when the upper set of beams is heated by the corresponding electrothermal heater, the beams bend in the desired direction due to thermal expansion, and the rest of the structure is pulled towards the positive direction of the axis (Fig. 1-b). In a similar manner, displacements in the negative direction are obtained by heating the lower beams.

During the operation of the MEMS nanopositioner, a bias voltage is applied to the integrated electrothermal sensors, which consist of two polysilicon heaters (per axis) positioned underneath the stage. Joule heating causes these heaters to reach a temperature of several hundred degrees Celsius, resulting in heat being conducted from the heaters to the stage via a small air gap (Fig. 1-c). The movement of the stage creates a change in the overlap between the stage and the heaters, affecting the rate of heat conduction between the two bodies. This results in small changes in the temperature of each heater, and due to the temperature-dependent resistivity of silicon, this creates detectable changes in the resistance of each heater. These resistance variations can be transformed into a measurable voltage and amplified to represent a measurement of the displacement of the stage. Two heaters are utilized per axis in a differential configuration, which helps to improve factors such as the linearity of the sensor output, and to reduce the effect of undesirable factors such as sensor aging and ambient temperature [6], [20].

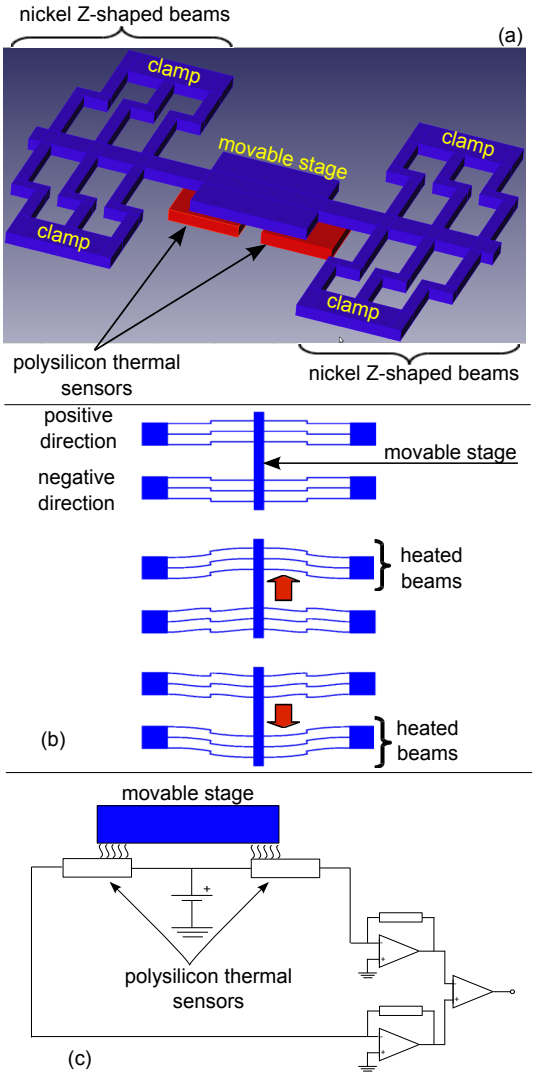

Fig. 1: (a): Simplified CAD schematic of one axis. (b): Principle of actuation in one axis. (c): Principle of the sensor operation in one axis.

B. Design of the stage

The above principle of motion was extended to two DoF (x and y axes), with separate actuators being implemented for the positive and negative directions along each axis. The MEMSCAP MetalMUMPs MEMS fabrication process was used to fabricate the MEMS device [21]. Fig. 2 displays a scanning electron microscope (SEM) image of the fabricated 2-DoF nanopositioner. Its fabricated size including the actuators and sensors is approximately $3mm \times 3mm$, with the movable stage being approximately $1mm \times 1mm$ in size. For each actuator, three Z-shaped beams are used in parallel to increase the actuating force used to move the stage. A series of beam flexures located at the corners of the stage are used to mechanically guide the motion of the stage and to minimize the cross-couplings between the x axis and the y axis during operation. The cross-section of the beams was designed to be small such that the heat transfer from one actuator to another actuator or to the stage is as small as possible. The beam flexures and the Z-shaped beams comprising the actuators have

cross-section dimensions of $8\mu m \times 20\mu m$ (width $\times$ height).

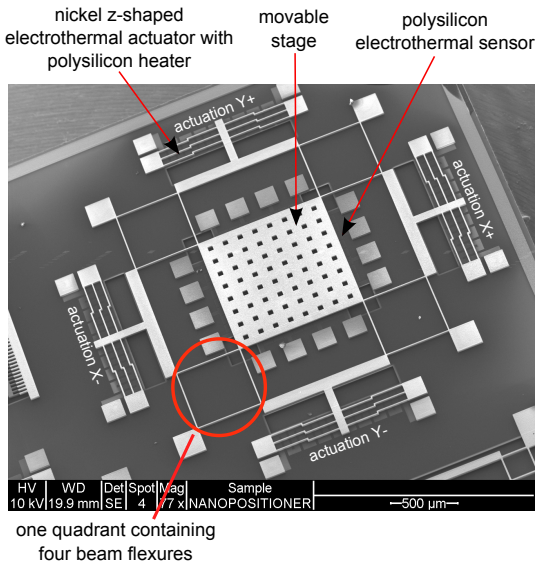

Fig. 2: SEM image of the 2-DoF MEMS nanopositioner.

C. Characterization of the electrothermal actuators and sensors

1) Characterization of the sensors: First, the electrothermal sensors integrated in the MEMS device are characterized. The objective is to evaluate the relationship between the actual displacement x (resp. y) of the movable stage and the output voltages from the sensors. The experiment is performed as follows. A constant input voltage $U_x = 50V$ (resp. $U_y = 50V$) is applied to the actuators along the x-axis (resp. along the y-axis) of the nanopositioner. Then, a Polytec MSA-400 Micro System Analyzer (MSA) is used to directly measure the actual displacement x (resp. y) of the device's moving structures. At the same time, the sensor readout circuit presented in Fig. 1-c, consisting of a pair of transimpedance amplifiers and a differential amplifier, is used to provide the sensor output voltages. This is repeated for different values of the voltages: $U_{x,y} \in \{-150, -125, -100, -75, -50, 0, 50, 75, 100, 125, 150\}$. Finally, the actual displacement x (resp. y) measured by the MSA is plotted versus the output voltage of the sensor of the x-axis (resp. the output voltage of the sensor of the y-axis), which ranges from $-4V$ to $8V$. The results are shown in Fig. 3. From these results, we infer that a linear function can be used to sufficiently capture the sensors' behavior. A more complex sensor model (e.g. a model using high order polynomials) can also be used to increase the model accuracy, however a model order greater than 6 is required to substantially decrease the standard deviation between the simulated sensor model and the experimental curves. We have therefore used a linear function, which is shown to give a good compromise between model simplicity and a low standard deviation. From Fig. 3, we remark that the linear gain of the positive direction is different from the gain of the negative direction for each of the x and y axes. This may be due to non-ideal positioning of the two heaters underneath the stage in the fabricated device, making the measurement asymmetrical in the two directions of each axis. Nevertheless, this asymmetry can be compensated by adjusting the amplifier gains or by using convenient inverse gains that enable the displacements x and y to be traced back from the sensors' output voltages. Later in this paper, these inverse gains are used such that the whole system studied has the control voltages U_x and U_y as the input while the output is the displacements x and y.

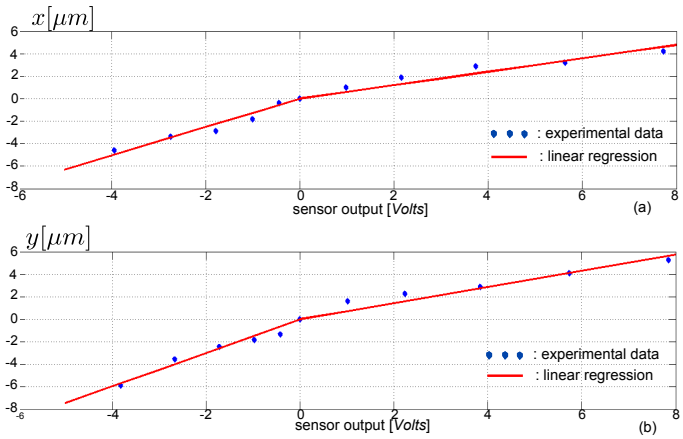

Fig. 3: Sensor characteristics: displacement versus the output voltage of the sensor.

2) Characterization of the input-output map of the MEMS nanopositioner: Here, we characterize the static behavior of the fabricated 2-DoF MEMS nanopositioner, i.e. the map that links the input control voltages U_x and U_y with the output displacements x and y. To achieve this, a triangular input voltage U_x is first applied while maintaining $U_y = 0$. The generated output displacement x is reported and the input-output map (U_x, x) is plotted (see Fig. 4-a). This corresponds to the direct transfer on the x axis. At the same time, the effect of U_x on the y displacement is reported and the map (U_x, y) is plotted (see Fig. 4-c). This corresponds to the coupling effect with the y axis. Next, a triangular input voltage U_y is applied and the voltage U_x is set to zero. Similarly to the previous characterization, the generated output displacement y is reported and the (U_y, y) map is plotted in order to obtain the direct transfer on the y axis (see Fig. 4-d). Finally the input-output map (U_y, x) provides the coupling with the x axis (see Fig. 4-b). We note that several cycles of the triangular input voltages U_x (and U_y) were applied and utilized to obtain the results plotted in Fig. 4. These figures show a good correlation between the curves from the different cycles and consequently demonstrate the repeatability of the voltage $\rightarrow$ displacement behavior.

The frequency of the used triangular signals should be low enough to avoid the influence of the system dynamics on the input-output characteristics, which is static. This influence is called the phase-lag and should not affect any static characterization. A variety of tests allow us to see that for a frequency lower than $0.1Hz$, the phase-lag is negligible. The results in Fig. 4 have been obtained with a frequency of $0.05Hz$.

From these figures, we conclude that: i) the 2-DoF MEMS nanopositioner possesses a nonlinear static behavior, and ii) the device has some undesired coupling $U_x \rightarrow y$ and $U_y \rightarrow x$.

These nonlinearities are largely due to the nonlinear phenomena in the resistivity and thermal coefficients of the polysilicon heaters within the actuators and sensors [22]. On the other hand, the cross-couplings are mechanical in nature and largely result from the thermal transfer from the actuator of the x axis (resp. y axis) to the Z-shaped beams of the y axis (resp. x axis) through the beam flexures. These cross-couplings can also be attributed to structural asymmetries that result from the limited precision of the microfabrication process used. These nonlinearities and couplings will be controlled using a combined feedback-feedforward controller in the following sections. Also, Fig. 4 shows that displacement ranges in excess of $\pm 5\mu m$ for the x and y axes are achievable. These ranges are comparable to the ranges obtained with classical nanopositioners such as piezotubes in atomic force microscopy [23], [24]. It is worth mentioning that the responses along the x-axis are noticeably different from the responses along the y-axis, in particular for the cross-coupling. These differences are due to imperfections inherent in the nanopositioner itself, such as the aforementioned structural asymmetry, which leads to slightly differing mechanical and thermomechanical behavior between the two axes.

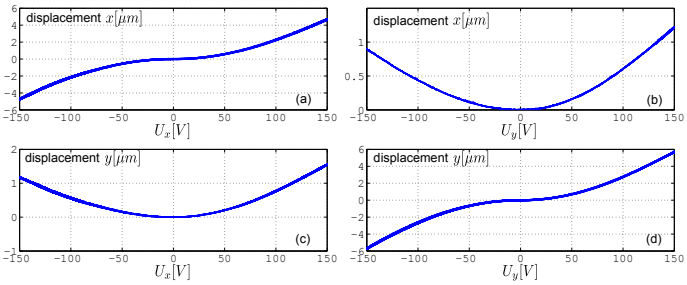

Fig. 4: Output displacement versus input voltage (static characteristic), obtained with $f = 0.05Hz$.

It should be noted that the resolution offered by the MEMS device is well suited for nanopositioning applications. Indeed, when applying lower actuation voltages, in particular in the range $-50V \leq U_i \leq 50V$ (with $i = \{x, y\}$), displacements on the order of hundreds of nanometers are possible, as shown in Fig. 5.

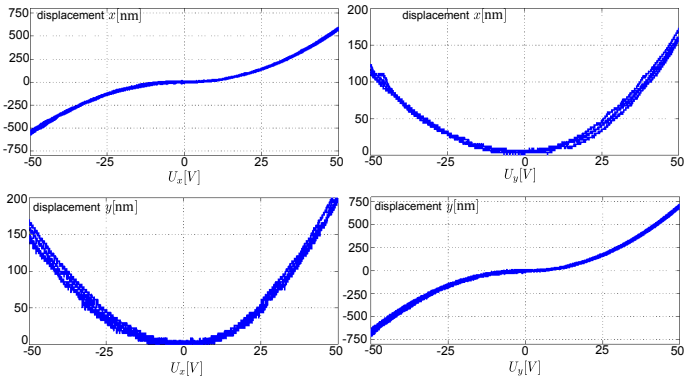

Fig. 5: Static characteristic when using lower actuation voltages ($-50V \leq U \leq 50V$).

We have mentioned above that the static characteristic depicted in Fig. 4 was carried out using a low-frequency sine input signal. This was done to avoid experiencing phase-lag. In order to explore this effect, we have performed further characterization of the input-output map when a higher-frequency input is used. We have used frequencies of both $1Hz$ and $5Hz$ for this purpose, and the corresponding input-output maps are shown in Fig. 6. As these figures clearly show, the phase-lag imparts a hysteresis-like effect to the initial curves depicted in Fig. 4-a and d. The deformation of these curves results from the phase difference between the input voltage and the output displacement, and is seen when the input rate is increased. Such lag is to be avoided when the static characteristic is to be characterized.

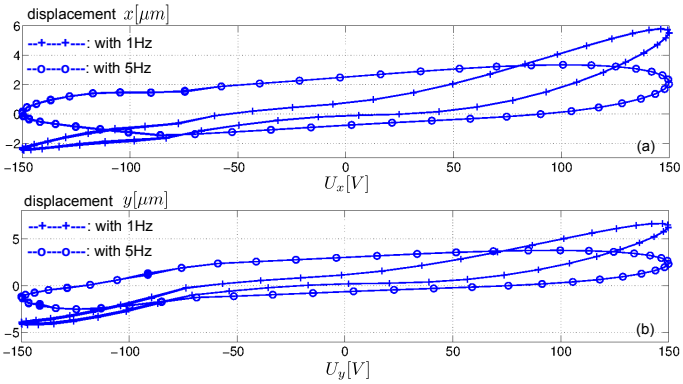

Fig. 6: Output displacement versus input voltage obtained with higher frequency inputs ($f = 1Hz$ and $f = 5Hz$): the phase-lag effect.

3) Frequency response of the MEMS nanopositioner: The previous subsection provided the static characteristics of the 2-DoF MEMS nanopositioner. To evaluate its dynamics, we perform a frequency analysis. Fig. 7 displays the results from which the direct transfer functions and the cross-couplings can be evaluated. The results show that the bandwidth of the MEMS device, which is similar for the two axes x and y, is about $3Hz$. As we remark from the figure, the open-loop frequency response does not show any mechanical resonant modes and has a low-pass filter characteristic. This is due to the limited bandwidth of the thermal actuation mechanism relative to the bandwidth of the mechanical structure. This means that the overall bandwidth of the system is insufficient to excite the mechanical resonant modes of the nanopositioner. A modal simulation of the nanopositioner performed using finite element analysis shows that the first resonant mode is an out-of-plane mode at $4.9kHz$, while the in-plane modes are located at approximately $9.4kHz$.

4) Conclusions from the experimentally-obtained characteristics: The 2-DoF MEMS nanopositioner shows nonlinear behavior in its static response (Fig. 4) and cross-couplings in both static (Fig. 4-b and c) and dynamic (Fig. 7-b and c) responses. These nonlinearities and cross-couplings limit the device's open-loop accuracy despite its potential for high resolution positioning. Thus, a closed-loop control technique is required to reject the cross-couplings and to enhance its static and dynamic performance. The following sections will be focused on the development of a feedforward and feedback

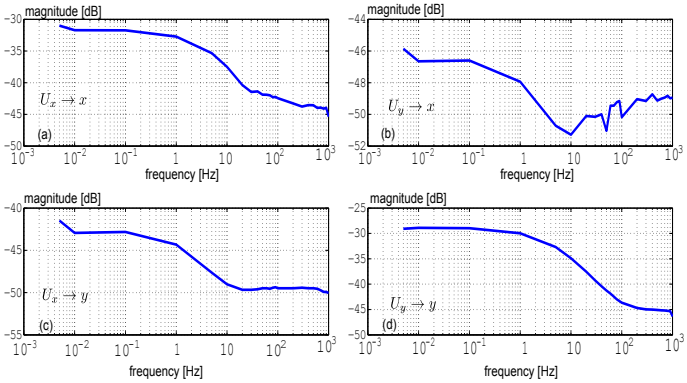

Fig. 7: Frequency response of the 2-DoF MEMS nanopositioner.

control system for this purpose. While the feedforward control scheme is first used to linearize the static nonlinearities, the feedback scheme is employed to enhance the overall performance of the system which encompasses its tracking capability, accuracy, and the rejection of the coupling effects. Fig. 8 depicts the equivalent block diagram of the 2-DoF MEMS device from which the control synthesis shall start.

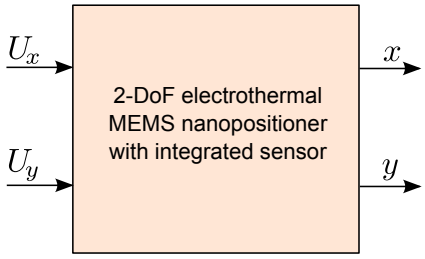

Fig. 8: Block diagram of the 2-DoF MEMS nanopositioner.

III. Feedforward Control and Modeling

The aim of the feedforward control presented here is to derive a linear system by compensating the static nonlinearities. After the linearization, a linear model is developed and will be used for the design of a feedback controller in the next section.

A. Feedforward control and linearization

Let us consider the block diagram in Fig. 9 where a feedforward controller (or compensator) denoted Γ_x^i (resp. Γ_y^i) is implemented on the x axis (resp. y axis). In the figure, x_{rf} and y_{rf} represent the inputs of the compensators.

One way to determine the required compensators is by first finding a model that approximates the behavior between the input U_x (resp. U_y) and the output x (resp. y) as depicted in Fig. 4-a (resp Fig. 4-d), and then inverting this model to derive the (x_{rf}, U_x) (resp. (y_{rf}, U_y)) map such that we obtain $x = x_{rf}$ (resp. $y = y_{rf}$). This method is less desired as it requires an invertible model. Furthermore, two calculations are done with this method: the calculation of the model itself first, and then the derivation of the controller from the model.

Another way of calculating the compensators Γ_x^i and Γ_y^i is by constructing the maps (x, U_x) and (y, U_y) from the experimental data instead of (U_x, x) and (U_y, y), and then by calculating the compensators from these maps by letting $x_{rf} = x$ and $y_{rf} = y$. The main advantage of this method is that the modeling and the related conditions (invertibility, etc.) are bypassed. We shall use this method to derive the compensators Γ_x^i and Γ_y^i.

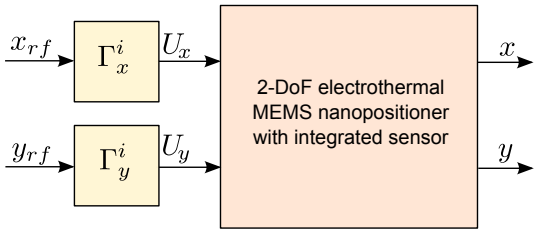

Fig. 9: Block diagram of the 2-DoF MEMS nanopositioner with the feedforward controllers.

Consider the (x_{rf}, U_x) and (y_{rf}, U_y) maps from the experimental data as shown in Fig. 10 (xxx-plot). Remember that that Fig. 10-a (resp. Fig. 10-b)) is the inverted plot of Fig. 4-a (resp. Fig. 4-b). An initial structure that comes to mind to approximate this map is a polynomial function. However, further tests show that a high polynomial degree (more than 15) is required to closely match the experimental data. Not only is the compensator excessively complex with such a structure but also it appears that if the input reference x_{rf} or y_{rf} is extended slightly outside the range of identification, which is nearly $\pm 5\mu m$, the output voltage of the compensator quickly diverges and the MEMS actuators are subjected to very high voltages which may damage them. Therefore, we propose here a structure based on a hyperbolic arcsine function which, after different tests, shows that such divergence is avoided. For this aim, we consider the following more generalized structure of the compensators:

$$\begin{cases} U_x(k) = \Gamma_x^i\left(x_{rf}(k)\right) \\ U_y(k) = \Gamma_y^i\left(y_{rf}(k)\right) \end{cases} \Updownarrow \begin{cases} U_x(k) = c_{1x}x_{rf}(k) + c_{2x}\sinh^{-1}\left(c_{3x}x_{rf}(k) + c_{4x}\right) \\ U_y(k) = c_{1y}y_{rf}(k) + c_{2y}\sinh^{-1}\left(c_{3y}y_{rf}(k) + c_{4y}\right) \end{cases} \quad (1)$$

where c_{1j} $(j = x, y)$ is a coefficient for the affine term of the structure and c_{2j}, c_{3j} and c_{4j} are the coefficients for the hyperbolic arcsine term. The reason why we introduce the affine term is to improve the accuracy of the compensators' models based on the hyperbolic arcsine when the range of inputs x_{rf} and y_{rf} is high. Indeed, the hyperbolic arcsine is very accurate at the low range of inputs x_{rf} and y_{rf} (within $\pm 1\mu m$) and marginally loses accuracy outside this range. The affine term can compensate for this loss of accuracy outside $\pm 1\mu m$.

The identification of the compensators' coefficients is carried out with the following least-square based optimization problem:

$$\begin{cases} \min\limits_{(c_{1x},c_{2x},c_{3x},c_{4x})\in\mathbb{R}^4} \sum\limits_{k=1}^{N_{\exp}} \left(U_x^{data}(k) - U_x(k)\right)^2 \\ \min\limits_{(c_{1y},c_{2y},c_{3y},c_{4y})\in\mathbb{R}^4} \sum\limits_{k=1}^{N_{\exp}} \left(U_y^{data}(k) - U_y(k)\right)^2 \end{cases} \quad (2)$$

where $U_x(k)$ and $U_y(k)$ are defined by the equations in (Eq. 1). The employed inputs $x_{rf}(k)$ and $y_{rf}(k)$ of (Eq. 1) are the experimental data $x(k)$ and $y(k)$ such that: $x_{rf}(k) = x(k)$ and $y_{rf}(k) = y(k)$. U_x^{data} and U_y^{data} are the voltages measured experimentally (the triangular signals) and N_{exp} is the length of the experimental data. After identification, we obtain:

$$\begin{pmatrix} c_{1x} \\ c_{2x} \\ c_{3x} \\ c_{4x} \end{pmatrix} = \begin{pmatrix} 16.4 \\ 14.65 \\ 16.17 \\ 0.029 \end{pmatrix}; \quad \begin{pmatrix} c_{1y} \\ c_{2y} \\ c_{3y} \\ c_{4y} \end{pmatrix} = \begin{pmatrix} 13.77 \\ 14.19 \\ 14.14 \\ 0.057 \end{pmatrix} \quad (3)$$

Fig. 10 shows the simulation of the compensators (x_{rf}, U_x) and (y_{rf}, U_y) (solid-line plot) compared with the experimental results (xxx-plot), with a close match between them being evident.

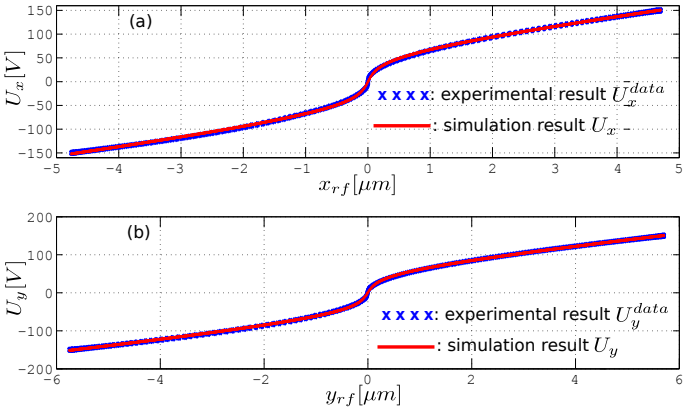

Fig. 10: The compensators $U_x(k) = \Gamma_x^i\left(x_{rf}(k)\right)$ and $U_y(k) = \Gamma_y^i\left(y_{rf}(k)\right)$: experimental result compared with the simulation result.

B. Experimental results

The compensators Γ_x^i and Γ_y^i defined in (Eq. 1) with the identified parameters are implemented according to the diagram in Fig. 9, and the linearity of the compensated system is checked. First, a triangular input reference x_{rf} with an amplitude of $5\mu m$ and a frequency $f = 0.05Hz$ (equal to the identification frequency) is applied. Fig. 11-a shows the yielded displacement along the x axis (direct transfer) while Fig. 11-c shows its influence on the y axis (coupling). Then, x_{rf} is set to zero and a triangular input reference y_{rf} with the same amplitude and frequency as before is applied. Fig. 11-d shows the obtained displacement along the y axis while Fig. 11-b is the coupling with the x axis. From these figures, we conclude that the 2-DoF nanopositioner was linearized in both axes with slopes (gains) close to $1\frac{\mu m}{\mu m}$ (see Fig. 11-a and d). The cross-couplings still exist however (Fig. 11-b and c), and to reduce them we propose adding a feedback control scheme. This feedback technique will also be used to reject other external disturbances, such as an interaction force during a nanopositioning task. Finally, a further aim of the feedback control is to enhance the performance of the MEMS nanopositioner in terms of accuracy and response time. To enable the design of the feedback control scheme, we first model the linearized system.

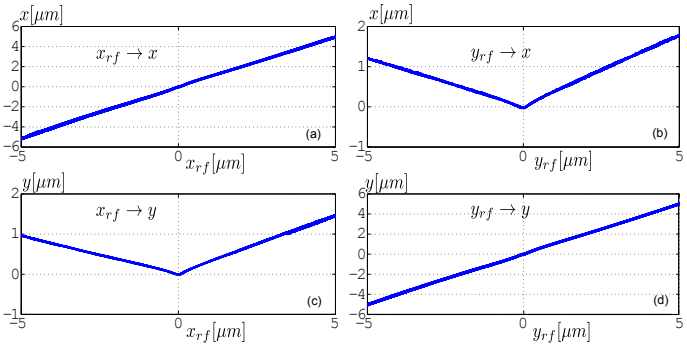

Fig. 11: Input-output map when using the nonlinearity compensators.

C. Modeling the linearized system

The system to be modeled is the 2-DoF MEMS nanopositioner augmented by the compensators, i.e. the linearized system pictured in Fig. 9. Its static characteristics are presented in Fig. 11 and its dynamics, that we denote $D_x(s)$ and $D_y(s)$ for the x and y axis respectively, can be identified from an experimental step response or a frequency response. In order to derive a simple model that is complete enough for a controller design, we propose considering the cross-couplings as disturbances. Therefore, we use the following model:

$$\begin{cases} x = k_x D_x(s) x_{rf} + d_x \\ y = k_y D_y(s) y_{rf} + d_y \end{cases} \quad (4)$$

where k_x and k_y are the static gains close to unity and which can be identified from Fig. 11-a and d respectively, and d_x and d_y are the couplings $y_{rf} \to x$ and $x_{rf} \to y$ respectively. Notice that these couplings are not constant as they include the static part identifiable from Fig. 11-b and c and a dynamic component identifiable from a step response or a harmonic analysis.

To identify the dynamics and static gain $k_x D_x(s)$ (resp. $k_y D_y(s)$) together, a step input reference $x_{rf} = 5\mu m$ (resp. $y_{rf} = 5\mu m$) is used. Then we employ an ARMAX parametric identification technique in MATLAB [25] such that the model will match with experimental data. Different model orders (with and without zeros) were identified, simulated and compared with the experimental data. They show that second order models, with two zeros for each model, provided the best fit with the experimental data while maintaining a simple structure (low order). The presence of the two zeros increases

the accuracy of the models during the transient part of the response.

$$\begin{cases} k_x D_x(s) = \frac{5.6\times10^{-3}(s+5019)(s+5.9)}{(s+38.86)(s+4.3)} \\ k_y D_y(s) = \frac{6.7\times10^{-3}(s+5022)(s+15.5)}{(s+49.9)(s+10.5)} \end{cases} \quad (5)$$

Notice that the dynamics D_x and D_y can be extracted from (Eq. 5) by replacing the static gains k_x and k_y by their numerical values identified from Fig. 11-a and d respectively. Fig. 12 displays the comparison between the identified models (Eq. 5) and the experimental step responses, and demonstrates the accuracy of the models.

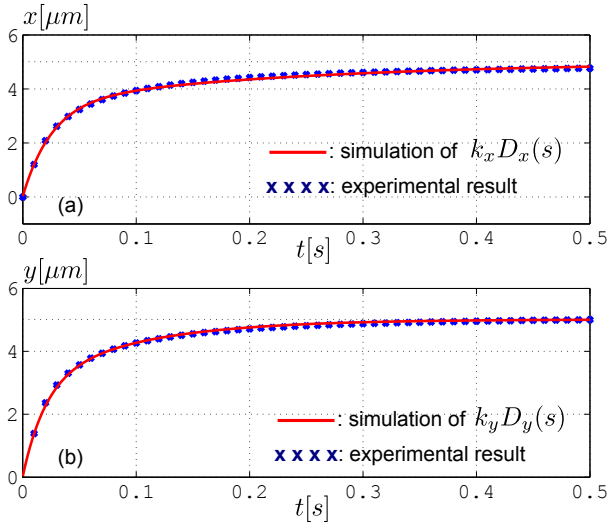

Fig. 12: Step response of the compensated system: (a) with $x_{rf} = 5\mu m$, (b) with $y_{rf} = 5\mu m$.

IV. IMC-FEEDBACK CONTROL

The previous section focused on the feedforward control of the 2-DoF MEMS nanopositioner in order to derive a general linearized system. The developed and identified models of the linearized system are given by (Eq. 4) and (Eq. 5). The aim of this section is to construct and design a feedback controller for the previous system in order to reject the couplings d_x and d_y inherent in the fabricated MEMS device, to reject the effects of external disturbances (interaction forces, etc.), and to enhance performance characteristics such as tracking accuracy and response time. The development of feedback control techniques for integrated multi-DoF micro/nanopositioning systems has recently been attracting considerable attention [26]–[29]. Recently [30], we have demonstrated that simple and robust enough controllers could be obtained for piezoelectric micro/nanopositioning systems by using an IMC feedback scheme. The controllers derived using these approaches can efficiently reject the cross-couplings, account for any model uncertainties and still maintain the expected performance. This is therefore very convenient for the models of the linearized 2-DoF MEMS device presented in (Eq. 4). Furthermore, the computation of the controller itself is simple and is almost immediate as soon as a model is available.

A. Control principle

The principle of an IMC approach is based on incorporating an approximate model of the system in the controller. A well known example of an IMC approach is the Smith predictor, where an approximate model containing an approximate delay is contained in the control system [31]. Most IMC schemes place the approximate model in parallel with the process. Hence, the feedback is constructed from the error between the process's output and the approximate model's output. As we will further demonstrate, such a scheme permits disturbances rejection and good robustness relative to uncertainties. Consider Fig. 13-a which represents the diagram of the 2-DoF MEMS nanopositioner, the feedforward controllers Γ_x^i and Γ_y^i for the linearization, and a feedback scheme based on the IMC approach. In this figure, x_r and y_r are the reference inputs for the closed-loop. The IMC feedback control system is composed of: 1) the approximate models $\hat{G}_x(s)$ and $\hat{G}_y(s)$ in parallel with the linearized process, and 2) the controllers $C_x(s)$ and $C_y(s)$ which are cascaded with the process. As approximate models, we use:

$$\begin{cases} \hat{G}_x(s) = k_x D_x(s) \\ \hat{G}_y(s) = k_y D_y(s) \end{cases} \quad (6)$$

Remember that the linearized process, that we simply call the real process or process, has the following structure:

$$\begin{cases} x = G_x(s)x_{rf} + d_x \\ y = G_y(s)y_{rf} + d_y \end{cases} \quad (7)$$

where $G_x(s)$ and $G_y(s)$ are the real processes without the disturbances (cross-couplings) d_x and d_y respectively. The difference between $G_x(s)$ and $G_y(s)$ relative to (Eq. 6) is the uncertainties in $k_x D_x(s)$ and $k_y D_y(s)$. A desirable property of the IMC approach is its ability to account for such uncertainties as well the disturbances to be rejected. Fig. 13-b represents the equivalent diagram of Fig. 13-a when using the process equation in (Eq. 7).

In the following section, we only analyze and synthesize the controller for the x axis knowing that the process for the y axis is the same. From the approximate model (Eq. 6), the real model (Eq. 7), and the block diagram in Fig. 13-b, we yield the equation relating the reference x_r, the output to be controlled x, and the disturbance d_x that is assumed to encompass the cross-couplings and other external perturbations:

$$x = \frac{G_x C_x}{\left(1 + C_x\left(G_x - \hat{G}_x\right)\right)} x_r + \frac{\left(1 - \hat{G}_x C_x\right)}{\left(1 + C_x\left(G_x - \hat{G}_x\right)\right)} d_x \quad (8)$$

The synthesis of the controller $C_x(s)$ will be based on this equation.

B. Controller synthesis

Let us first choose $C_x(s) = \frac{1}{\hat{G}_x(s)}$ and introduce that into (Eq. 8). After simplification, we obtain:

$$x = 1 \cdot x_r + 0 \cdot d_x \quad (9)$$

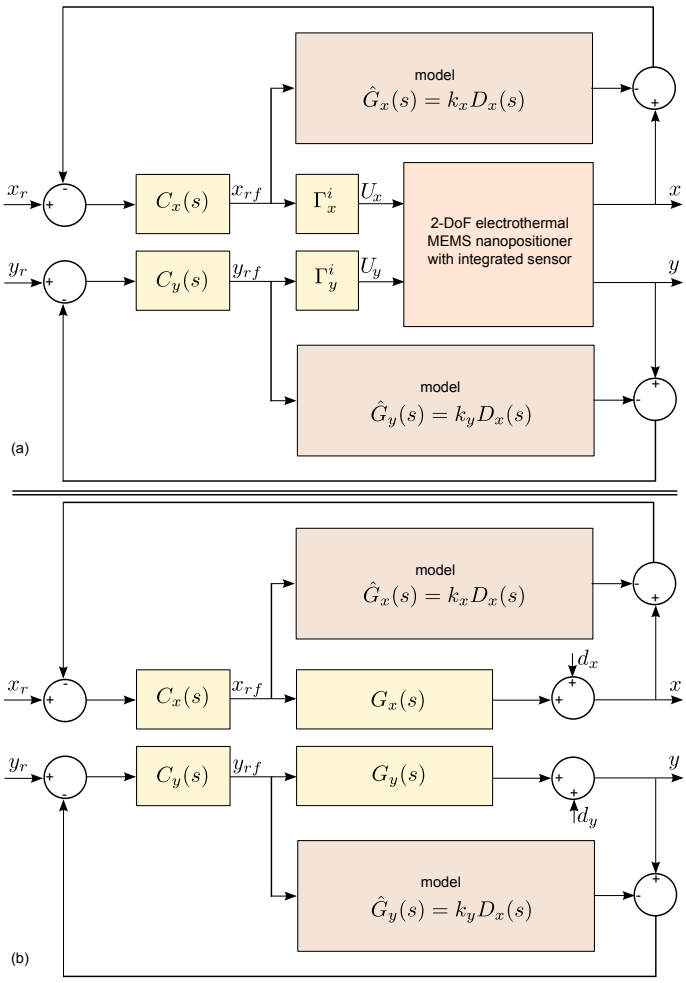

Fig. 13: Block diagram of the feedforward and IMC-feedback control of the 2-DoF electrothermal MEMS nanopositioner.

From (Eq. 9), we conclude that the accuracy is always maintained ($x = x_r$) and the disturbance is always rejected ($x = 0 \cdot d_x$), for any input reference x_r, any disturbance d_x and any approximate model $\hat{G}_x(s)$. However, (Eq. 9) is valid in a steady-state regime only. Consequently choosing the controller to be $C_x(s) = \frac{1}{\hat{G}_x(s)}$ only improves the static regime and the transient part is not handled. To consider the transient part (or dynamics), we slightly modify the controller by adding a filter $F_x(s)$ such that:

$$C_x(s) = \frac{1}{\hat{G}_x(s)} F_x(s) \tag{10}$$

Consider first the case where we have a perfect model: $G_x(s) = \hat{G}_x(s)$. Then, introducing this perfect model in (Eq. 10) and introducing the result into (Eq. 8) yields:

$$x = F_x(s) x_r + (1 - F_x(s))\, d_x \tag{11}$$

According to (Eq. 11), the filter $F_x(s)$ should be chosen as a reference model for the closed-loop transfer function $\frac{x(s)}{x_r(s)}$. For instance, if we specify a closed-loop response without overshoot and with a response time less or equal to t_{xr}, a first order reference model with a time constant $\tau_x = 3t_{xr}$ can be used and the filter becomes:

$$F_x(s) = \frac{1}{1 + \tau_x s} \tag{12}$$

The reason for setting the static gain of the filter equal to one ($F_x(s = 0) = 1$) is to ensure disturbance rejection and to ensure the tracking performance at the steady-state regime (static precision). Indeed, letting $F_x(s = 0) = 1$ in (Eq. 11) permits us to maintain the results in (Eq. 9) at $s = 0$, i.e. as $t \to \infty$. We note that according to the final value theorem (see for instance [32]), when the input signals $x_r(t)$ and $d_x(t)$ are constant, the calculation of the final value of the output $x(t)$, i.e. calculation of $x(t \to \infty)$, comes back to the calculation of $x(s)$ in (Eq. 11), letting $s = 0$ in the transfer functions in (Eq. 11) and (Eq. 12) and replacing $x_r(s)$ and $d_x(s)$ by their constants.

Consider now that the model $\hat{G}_x(s)$ is not perfect, i.e. $\hat{G}_x(s) \neq G_x(s)$. We have:

$$x = \frac{\frac{G_x}{\hat{G}_x} F_x}{\left(1 + F_x \left(\frac{G_x}{\hat{G}_x} - 1\right)\right)} x_r + \frac{(1 - F_x)}{\left(1 + F_x \left(\frac{G_x}{\hat{G}_x} - 1\right)\right)} d_x \tag{13}$$

In (Eq. 13), we still conclude that the disturbance is always rejected and the static precision still maintained. Indeed, by introducing the proposed filter (Eq. 12) in the new closed-loop equation (Eq. 13) and letting $s = 0$ (i.e. $t \to \infty$), we obtain the result in (Eq. 9). To analyze the dynamics, or transient element, examining the structure of the closed-loop equation (Eq. 13) permits the following conclusions to be made (assuming that $G_x(s)$ and $\hat{G}_x(s)$ have the same structure, i.e. polynomials of the same degree):

- the more the parameters of $\hat{G}_x(s)$ differ from the parameters of $G_x(s)$, the less the closed-loop transfer function $\frac{x(s)}{x_r(s)}$ tracks the reference model $F_x(s)$ in the transitory regime,
- and the closer the parameters of $\hat{G}_x(s)$ are to the parameters of $G_x(s)$, the closer the transitory regime of the closed-loop transfer function $\frac{x(s)}{x_r(s)}$ is to that of the reference model $F_x(s)$.

To summarize, the controller $C_x(s)$ is chosen to be equal to (Eq. 10) where $F_x(s)$ is the reference model for the closed-loop system $\frac{x(s)}{x_r(s)}$. The ability of the closed-loop system to track the reference model during the transitory regime depends on the error amplitudes (or uncertainties) between the approximate model $\hat{G}_x(s)$ and the real model $G_x(s)$. However, the IMC feedback scheme always ensures disturbance and cross-coupling rejection for any uncertain model $\hat{G}_x(s)$, any disturbance d_x, and any reference input x_r. Furthermore, it always ensures static precision, i.e. $x = x_r$ at $t \to \infty$.

C. Experimental results of the closed-loop system

The IMC feedback control system has been implemented to control the linearized 2-DoF MEMS nanopositioner. A computer with MATLAB-SIMULINK software operating with a refresh time of $1ms$ was used to implement the feedforward

controllers (Γ_x^i and Γ_y^i) and the IMC feedback control system. A dSPACE acquisition board is employed as the interface between the computer and the rest of the setup (Fig. 14). A high voltage (HV) amplifier with $\pm 200V$ range amplifies the signals from the computer/dSPACE system which are used to drive the MEMS device. This HV amplifier is sufficient to drive the electrothermal actuators. Finally, the measurement of the displacements x and y for the feedback control are carried out using the integrated electrothermal sensors.

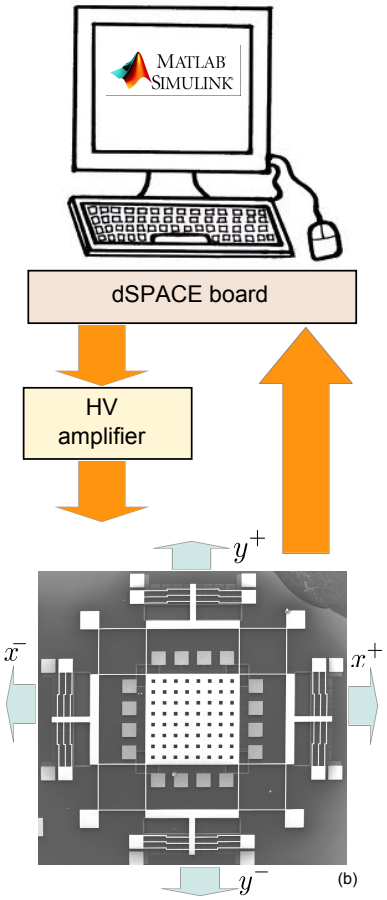

Fig. 14: Experimental setup.

For the experiments, we chose the filters $F_x(s)$ and $F_y(s)$ for the controllers $C_x(s)$ and $C_y(s)$ respectively such that the closed-loop has a response time of $t_{xr} = t_{yr} = 200ms$. Using (Eq. 10), (Eq. 12), (Eq. 6) and (Eq. 5) we have:

$$\begin{cases} C_x(s) = \frac{(s+38.86)(s+4.3)}{5.6\times10^{-3}(s+5019)(s+5.9)\left(1+\frac{0.2}{3}s\right)} \\ C_y(s) = \frac{(s+49.9)(s+10.5)}{6.7\times10^{-3}(s+5022)(s+15.5)\left(1+\frac{0.2}{3}s\right)} \end{cases} \quad (14)$$

Remember that the control system of the IMC feedback technique comprises the controllers $C_x(s)$ and $C_y(s)$ cascaded with the linearized process, and the approximate model $\hat{G}_x(s)$ and $\hat{G}_y(s)$ in parallel with it. Therefore, the final controllers implemented in MATLAB-SIMULINK encompass this IMC control system ($C_x(s)$, $C_y(s)$, $\hat{G}_x(s)$ and $\hat{G}_y(s)$) and the feedforward controllers Γ_x^i and Γ_y^i. This is represented in Fig. 13.

The first experiment consists in analyzing the step responses of the closed-loop system. Figs. 15-a and b show the results when a series of step references x_r and y_r are applied at different times. From the figures, we conclude that the outputs x and y closely track these references, and that the effect of x_r (resp. y_r) on the output y axis (resp. x axis) is observed but quickly rejected. Figs. 15-c and d display a zoomed view of the response of x and y respectively to a reference $x_r = 4\mu m$. We observe that the tracking performance of the x axis has a response time of about $100ms$ (Fig. 15-c) which is much better than the initial specification ($200ms$), and zero static error. Additionally, the response time required to reject the effect of x_r on y (cross-couplings/disturbances) is about $400ms$ (Fig. 15-d). Despite this slightly long response time, the static error due to the disturbance as $t \to \infty$ remains zero as predicted by the theory. In Figs. 15-e and f zoomed views of the responses of x and y respectively to a reference $y_r = 4\mu m$ are displayed. The response time for the tracking performance for the y axis is about $120ms$ (Fig. 15-f) which is also much better than the initial specifications, and the static error is again zero. We also observe that although there is a slightly long response time to reject the effect of y_r on x (about $410ms$ according to Fig. 15-e), the static error due to this disturbance again approaches zero. To conclude, the bandwidth of the nanopositioner with the feedback-feedforward controllers corresponds to $30Hz$ along the x-axis and to $25Hz$ along the y-axis (calculated from the above settling times). These results clearly demonstrate the improvement made in terms of dynamic performance relative to the performance of the nanopositioner alone, which has a bandwidth of $3Hz$.

In the second experiment, a circular spatial reference is applied to the 2-DoF MEMS nanopositioner in order to verify its ability to track a more complex trajectory in 2D space. The circular reference is obtained by applying the following parametric cosine and sine functions to x_r and y_r:

$$\begin{cases} x_r(t) = R\cos(2\pi f_r t) \\ y_r(t) = R\sin(2\pi f_r t) \end{cases} \quad (15)$$

where $R[\mu m]$ is the radius of the circle, $f_r[Hz]$ is the specified frequency of rotation of the nanopositioner's stage, and t is the time. Fig. 16 shows the results obtained with a radius of $R = 4\mu m$ and a frequency of $0.5Hz$. The results show good tracking from the MEMS nanopositioner. Different frequencies have been tested, which show that similarly good tracking is achieved for any frequency lower than $5Hz$.

In summary, the combination of a feedforward and IMC-feedback control scheme as proposed in this paper has yielded an important improvement in the performance of the fabricated MEMS nanopositioner, in particular regarding its tracking accuracy, settling time (and bandwidth), and cross-coupling rejection. In particular, these cross-couplings were considered as disturbances in this paper (see (Eq. 7)), which the feedback controllers were synthesized to reject (see (Eq. 9) and (Eq. 11) and the corresponding analysis).

While the control scheme proposed in this paper enables the use of linear feedback techniques to improve the performance of the nanopositioner, it is also possible to bypass the feedforward component (for linearization) and to directly apply

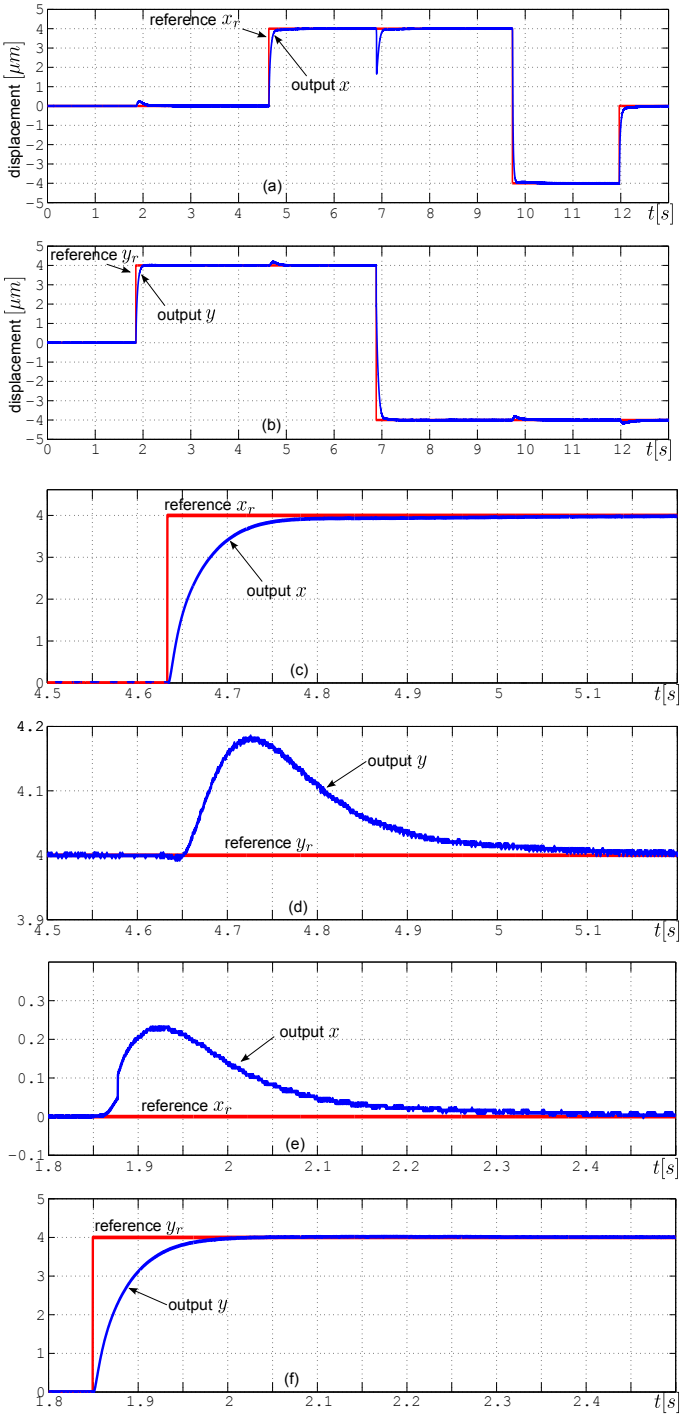

Fig. 15: Experimental responses of the closed-loop 2-DoF MEMS nanopositioner. (a) and (b): responses of x and y respectively to a series of step input references. (c) and (d): responses of x and y respectively to a step x_r. (e) and (f): responses of x and y respectively to a step y_r.

nonlinear controllers or gain-scheduled linear controllers. An advantage of these techniques is the potential for maintaining the same performance characteristics (response time, accuracy, etc.) of the nanopositioner over a large displacement range. However, these techniques require a more complex model and yield a more complex controller synthesis and implementation relative to the feedforward/linear-feedback scheme as proposed in this paper. This is a reason why, in the literature, feedforward-feedback schemes are often used to control precise positioning systems. Nevertheless, future work may involve synthesizing other control schemes for the MEMS nanopositioner.

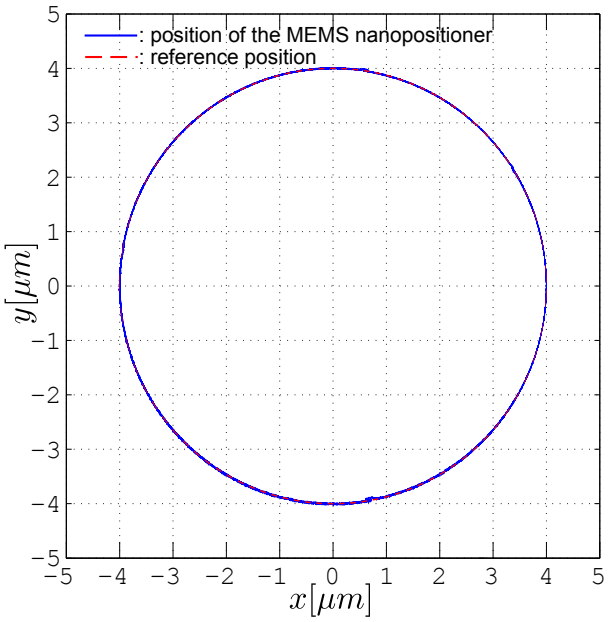

Fig. 16: Experimental responses of the closed-loop 2-DoF MEMS nanopositioner to a circular reference input.

V. Conclusion

This paper presented a fabricated 2-DoF MEMS nanopositioner with integrated electrothermal actuators and sensors, its full characterization, modeling, and control. The actuators, which are based on nickel Z-shaped beams, allow the device's stage to be positioned in the positive and negative directions along each axis, potentially making the design more useful than the classical V-shaped electrothermal actuators which are uni-directional in nature. Furthermore, relative to existing Z-shaped electrothermal actuators which are limited to one axis (x), the proposed design possesses two working axes (x and y). Another feature of the presented device is its completely integrated displacement sensing mechanism. Based on polysilicon resistors, the sensors can fully measure the stage displacements in the x and y directions. The characterization has demonstrated a range of displacement in excess of $\pm 5\mu m$ for both axes, and a response time of less than $300ms$. A feedforward control scheme for linearization combined with an IMC feedback scheme has been developed in order to reject cross-couplings between the two axes and to improve the general performance of the MEMS device, in particular its accuracy and response time. The main advantage of the proposed control scheme is the ease of derivation of the different controllers that it encompasses. The experimental results have demonstrated the effectiveness of the proposed controllers which allow the 2-DoF system to have good tracking performance with response times better than $110ms$, very high

accuracy and rejection of cross-couplings and disturbances. These results demonstrate the capabilities of the fabricated 2-DoF MEMS nanopositioner as part of a closed-loop system and its suitability for nanopositioning applications.

ACKNOWLEDGMENT

The authors would like to thank Dr. Yong Zhu (Griffith University, Australia) for his contributions to the design of an earlier version of this device. The SEM images were obtained with the assistance of the University of Newcastle's Electron Microscope and X-Ray Unit. This work was supported by the Australian Research Council.

REFERENCES

[1] G. Binnig and H. Rohrer, "The scanning tunneling microscope," *Scientific American*, vol. 253, pp. 50–56, 1986.

[2] S. M. Salapaka and M. V. Salapaka, "Scanning probe microscopy," *IEEE Control Systems Magazine*, vol. 28, no. 2, pp. 65–83, 2008.

[3] A. Pantazi, A. Sebastian, G. Cherubini, M. Lantz, H. Pozidis, H. Rothuizen, and E. Eleftheriou, "Control of MEMS-based scanning-probe data-storage devices," *IEEE Transactions on Control Systems Technology*, vol. 15, no. 5, pp. 824–841, 2007.

[4] M. Lantz, H. Rothuizen, U. Drechsler, W. Haberle, and M. Despont, "A vibration resistant nanopositioner for mobile parallel-probe storage applications," *Journal of Microelectromechanical Systems*, vol. 16, no. 1, pp. 130–139, 2007.

[5] S. Bergna, J. Gorman, and N. Dagalakis, "Design and modeling of thermally actuated MEMS nanopositioners," in *2005 ASME International Mechanical Engineering Congress and Exposition*, 2005, pp. 561–568.

[6] Y. Zhu, A. Bazaei, S. O. R. Moheimani, and M. R. Yuce, "Design, modeling, and control of a micromachined nanopositioner with integrated electrothermal actuation and sensing," *Journal of Microelectromechanical Systems*, vol. 20, no. 3, pp. 711–719, 2011.

[7] A. G. Fowler, A. N. Laskovski, A. C. Hammond, and S. O. R. Moheimani, "A 2-DOF electrostatically actuated MEMS nanopositioner for on-chip AFM," *Journal of Microelectromechanical Systems*, vol. 21, no. 4, pp. 771–773, 2012.

[8] N. B. Hubbard, M. L. Culpepper, and L. L. Howell, "Actuators for micropositioners and nanopositioners," *Applied Mechanics Reviews*, vol. 59, no. 6, pp. 324–334, 2006.

[9] C. Guan and Y. Zhu, "An electrothermal microactuator with Z-shaped beams," *Journal of Micromechanics and Microengineering*, vol. 20, no. 8, p. 085014, Aug. 2010.

[10] S.-C. Chen and M. L. Culpepper, "Design of contoured thermomechanical actuators and pulsing actuation to enhance dynamic performance," *Journal of Microelectromechanical Systems*, vol. 21, no. 2, pp. 340–349, Apr. 2012.

[11] J. Chow and Y. Lai, "Displacement sensing of a micro-electro-thermal actuator using a monolithically integrated thermal sensor," *Sensors and Actuators A: Physical*, vol. 150, no. 1, pp. 137–143, Mar. 2009.

[12] L. L. Chu and Y. B. Gianchandani, "A micromachined 2D positioner with electrothermal actuation and sub-nanometer capacitive sensing," *Journal of Micromechanics and Microengineering*, vol. 13, no. 2, pp. 279–285, Mar. 2003.

[13] T. Waterfall, K. Teichert, and B. Jensen, "Simultaneous on-chip sensing and actuation using the thermomechanical in-plane microactuator," *Journal of Microelectromechanical Systems*, vol. 17, no. 5, pp. 1204–1209, Oct. 2008.

[14] Y. Zhu, S. O. R. Moheimani, and M. R. Yuce, "Bidirectional electrothermal actuator with Z-Shaped beams," *IEEE Sensors Journal*, vol. 12, no. 7, pp. 2508–2509, Jul. 2012.

[15] J. Ouyang and Y. Zhu, "Z-Shaped MEMS thermal actuators: Piezoresistive self-sensing and preliminary results for feedback control," *Journal of Microelectromechanical Systems*, vol. 21, no. 3, pp. 596–604, Jun. 2012.

[16] M. Rakotondrabe, A. G. Fowler and S. O. R. Moheimani, "Characterization of a 2-DoF MEMS nanopositioner with integrated electrothermal actuation and sensing" in *IEEE Sensors 2012*, pp. 973-976, Taipei Taiwan, October 2012.

[17] A. Pantazi, M. A. Lantz, G. Cherubini, H. Pozidis, and E. Eleftheriou, "A servomechanism for a micro-electro-mechanical-system-based scanning-probe data storage device," *Nanotechnology*, vol. 15, no. 10, pp. S612–S621, Oct. 2004.

[18] Y. Zhu, S. O. R. Moheimani, and M. R. Yuce, "Simultaneous capacitive and electrothermal position sensing in a micromachined nanopositioner," *IEEE Electron Device Letters*, vol. 32, no. 8, pp. 1146–1148, 2011.

[19] M. A. Lantz, G. K. Binnig, M. Despont, and U. Drechsler, "A micromechanical thermal displacement sensor with nanometre resolution," *Nanotechnology*, vol. 16, no. 8, pp. 1089–1094, Aug. 2005.

[20] A. Sebastian, "Systems and control approach to electro-thermal sensing," in *Control Technologies for Emerging Micro and Nanoscale Systems*, E. Eleftheriou and S. O. R. Moheimani, Eds. Springer Berlin / Heidelberg, 2011, ch. 8, pp. 137–152.

[21] A. Cowen, R. Mahadevan, S. Johnson, and B. Hardy, "MetalMUMPs Design Handbook (Revision 3.0.)," 2009.

[22] A. Bazaei, Y. Zhu, S. O. R. Moheimani and M. R. Yuce, "Analysis of nonlinear phenomena in a thermal micro-actuator with a built-in thermal position sensor," *IEEE Sensors Journal*, vol. 12, no. 6, pp.1772–1784, June 2012.

[23] Y. K. Yong and S. O. R. Moheimani, "Vibration control of a novel tube scanner using piezoelectric strain-induced voltage," in *2009 IEEE/ASME International Conference on Advanced Intelligent Mechatronics*, Singpore, July 2009, pp. 1070–1075.

[24] S. Aphale, A. J. Fleming and S. O. R. Moheimani, "High speed nanoscale positioning using a piezoelectric tube actuator with active shunt control," *Micro & Nano Letters*, vol. 2, no. 1, pp. 9–12, Mar. 2007.

[25] L. Ljung, "System identification toolbox 7 user's guide," The Mathworks, Natick, MA USA, Oct. 2008.

[26] M. Rakotondrabe, K. Rabenorosoa, J. Agnus and N. Chaillet, "Robust feedforward-feedback control of a nonlinear and oscillating 2-DOF piezocantilever," *IEEE Transactions on Automation Science and Engineering*, vol. 8, no. 3, pp. 506–519, July 2011.

[27] C. Lee, G. Mohan, S. Salapaka, "2DOF control design for nanopositioning," in *Control Technologies for Emerging Micro and Nanoscale Systems*, Springer Berlin / Heidelberg, 2011, pp. 67–82.

[28] S. Bashash, N. Jalili, "Robust adaptive control of coupled parallel piezoflexural nanopositioning stages," *IEEE/ASME Transactions on Mechatronics*, vol. 14, no. 1, pp. 11-20, Feb. 2009.

[29] Y. K. Yong, K. Liu, S. O. R. Moheimani, "Reducing cross-coupling in a compliant XY nanopositioning stage for fast and accurate raster scanning," *IEEE Transactions on Control Systems Technology*, vol. 18, no. 5, pp. 1172–1179, Sept. 2010.

[30] M. Rakotondrabe, J. Agnus and P. Lutz, "Feedforward and IMC-feedback control of a nonlinear 2-DOF piezoactuator dedicated to automated micropositioning tasks," in *2011 IEEE Conference on Automation Science and Engineering (CASE)*, Trieste, Italy, Aug. 2011, pp. 393–398.

[31] K. J. Astrom, C. C. Hang and B. C. Lim, "A new Smith predictor for controlling a process with an integrator and long dead-time," *IEEE Transactions on Automatic Control*, vol. 39, no. 2, pp. 343–345, Feb. 1994.

[32] A. V. Oppenheim, A. S. Willsky and S. Hamid Nawab, *Signals & Systems*. New Jersey, USA. Prentice Hall. ISBN 0-13-814757-4.

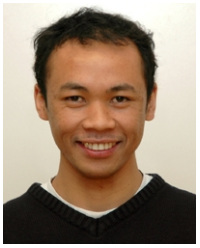

Micky Rakotondrabe graduated from the Institut Catholique des Arts et Métiers (ICAM engineering school, Lille France) in 2002, obtained the MSc on Control Systems from the Institut National des Sciences Appliquées (INSA, Lyon France) in 2003 and the PhD on Control Systems from the University of Franche-Comté at Besançon (UFC Besançon France) in 2006. His PhD research was led at FEMTO-ST Institute, Besançon France. He was assistant professor at UFC University and FEMTO-ST Institute in 2006-2007. Since sept 2007, he is associate professor at the same University and Institute. His research fields concern the design, modeling, signal estimation and control techniques for piezoelectric actuators in general and for microsystems.

Anthony G. Fowler was born in Taree, Australia. He received the Bachelor's degree in electrical engineering from the University of Newcastle, Callaghan, Australia, in 2010, where he is currently pursuing the Ph.D. degree in electrical engineering.

His research interests include the design and analysis of novel MEMS devices for energy harvesting and nanopositioning applications.

S. O. Reza Moheimani received his undergraduate degree in electrical engineering from Shiraz University in 1991 and completed his doctoral studies at University of New South Wales, Australia in 1996. In 1997 he joined University of Newcastle, Australia, embarking on a new research program addressing the dynamics and control design issues related to high-precision mechatronic systems. Professor Moheimani is the founder and director of Laboratory for Dynamics and Control of Nanosystems, a multimillion-dollar state-of-the-art research facility. His current research interests are mainly in the area of ultrahigh-precision mechatronic systems, with particular emphasis on dynamics and control at the nanometer scale, including applications of control and estimation in nanopositioning systems for high-speed scanning probe microscopy, modeling and control of microcantilever-based devices, control of microactuators in microelectromechanical systems, and design, modelling and control of micromachined nanopositioners for on-chip atomic force microscopy.

His work has been recognised by a number of awards including the IFAC Nathaniel B. Nichols Medal (2014); IFAC Mechatronic Systems Award (2013); IEEE Control Systems Technology Award (2009); Australian Research Council Future Fellowship (2009); IEEE Transactions on Control Systems Technology Outstanding Paper Award (2007); Australian Research Council Postdoctoral Fellowship (1999); and several best student paper awards in various conferences. He has served on the editorial boards of a number of journals, including the IEEE/ASME TRANSACTIONS ON MECHATRONICS, IEEE TRANSACTIONS ON CONTROL SYSTEMS TECHNOLOGY, and Control Engineering Practice. He has chaired several international conferences and workshops and currently chairs the IFAC Technical Committee on Mechatronic Systems. He has published over 270 refereed papers and five books and edited volumes. He is a Fellow of IEEE, IFAC and Institute of Physics (UK).